Supplementary Materials

A lightweight fabric-based adhesive winding actuator with high load capacity for slender rod-climbing robots

Zhouyi Wang[1,*], Liuwei Wang[2], Xiao Yin[1], Zhiyuan Weng[1], Yunlong Duan[1], Jiapeng Xie[1], Chenlu Xue[3], Zhendong Dai[1]

[1]College of Mechanical and Electrical Engineering, Nanjing University of Aeronautics and Astronautics, Nanjing 210016, Jiangsu, China.
[2]School of Mechanical Engineering, Nanjing University of Industry Technology, Nanjing 210023, Jiangsu, China.
[3]Faculty of Education and Liberal Arts, INTI International University, Nilai 71800, Malaysia.

[*]**Correspondence to:** Assoc. Prof. Zhouyi Wang, College of Mechanical and Electrical Engineering, Nanjing University of Aeronautics and Astronautics, Nanjing 210016, Jiangsu, China. E-mail: wzyxml@nuaa.edu.cn

Supplementary Section 1. The influence of actuator parameter changes on deformation with the simulation analysis

The parameters used in the analytical model—the length of the pleated region perpendicular to the pleats (L_k) and the unfolded length of the pleated bladder perpendicular to the pleats (L_a)—were introduced to replace discrete pleat-design variables such as the number of pleats (n), pleat height (h), pleat width (b), and pleat spacing (g). Consequently, the individual effect of each pleat-design parameter on actuator deformation was not examined separately in the initial analysis. Nevertheless, these parameters collectively determine both the detailed pleat geometry and the resulting deformation behavior of the actuator. Inspired by the distal musculature and skeletal organization of the chameleon tail, the pleat design followed the principle that individual pleats should not be excessively large, because oversized pleats would lead to discontinuous force output and increased moment arms. Instead, the preferred design trend was toward smaller and more densely distributed pleats, so as to maintain close conformity with the constraining-layer bladder. Accordingly, the number of pleats (n) should be as large as practicable, whereas the pleat height (h), pleat width (b), and pleat spacing (g) should be minimized within manufacturing limits. In practice, however, manufacturability must also be considered, since excessively small geometric features would impose stringent fabrication requirements and may become infeasible to produce. Based on these considerations, a parameter set satisfying the optimal deformation design criteria was selected as the baseline: pleat–bladder angle α=45°, bladder width w=20mm, bladder heat-sealing zone width c=4mm, pleat spacing g=5mm, pleat height h=3.9mm, and pleat width b=2.5mm. Using this baseline configuration, parameter-variation plots were generated to illustrate the influence of structural changes on actuator deformation.

Based on the ideal deformation criteria and the analytical deformation model, the effects of variations in individual structural parameters on actuator deformation were examined. As shown in Supplementary Figure 1A, when the bladder width (w) deviates from the design requirement, the winding morphology changes accordingly. Specifically, increasing the bladder width results in a larger inflated cross-section, which enlarges the radius of the circle enclosed by the constraining layer. This, in turn, reduces the winding central angle and decreases the actuator's effective operating range, particularly its ability to achieve stable adhesive winding around smaller-diameter objects. Conversely, decreasing the bladder width produces a narrower inflated cross-section, reduces the radius enclosed by the constraining layer, and increases the winding central angle. As a result, the actuator can achieve a greater number of winding turns, which is advantageous for adhesive winding around slender targets. However, the reduced bladder width also lowers structural stiffness and may therefore compromise adhesive-winding stability.

As illustrated in Supplementary Figure 1B, an increase in the angle α causes an increase in the radius of the cylindrical helix enclosed by the restraining layer. Subject to the minimum lead angle limit, the central angle of the cylindrical helix formed by the actuator upon deformation decreases. Consequently, although the actuator can still continue to curl and wrap, the adjacent coils of the helical bladder obstruct each other, preventing further deformation. When the angle decreases, the radius of the cylindrical helix enclosed by the restraining layer diminishes, and the corresponding central angle also decreases. In this scenario:

$$L_k' = \tan\alpha' \cdot \frac{(w-2c+c\pi)(L_a-L_k)}{\pi(w-2c)} \qquad \text{(S1)}$$

where α' is the modified angle between the pleats and the bladder. By comparing L_k' and L_k, it can be determined whether the cylindrical helix reaches the minimum lead angle limit. If $L_k' < L_k$ it indicates that the actuator deformation cannot reach the minimum lead angle limit; conversely, if $L_k' \geq L_k$ it indicates that it can. Given that $\alpha' < \alpha$, and $\alpha \in (0, \pi/2)$, we have $\tan\alpha' < \tan\alpha$. Therefore, $L_k' < L_k$. In summary, a decrease in the angle α leads to a smaller cylindrical helix radius upon deformation, a reduced winding central angle, and the inability of the actuator deformation to reach the minimum lead angle limit.

When the pleat height (h) increases, the overall bladder deformation changes only slightly. This is because once the deformation reaches the minimum-lead condition—that is, when the lead equals the inflated bladder length along the pleat direction—further deformation ceases. At that stage, the bladder has not yet fully unfolded: the upper layer remains partially unextended and residual pleating persists. The influence of this incomplete deformation state on actuator performance remains unclear and will be evaluated in future physical experiments. In contrast, when the pleat height decreases, the actuator can no longer achieve the intended deformed configuration. This is because a reduction in pleat height shortens the unfolded length of the pleated bladder measured perpendicular to the pleats, thereby reducing the difference between this length and the length of the pleated region perpendicular to the pleats. As a consequence, the central angle of the cylindrical helical deformation decreases, whereas the radius of the cylindrical helix enclosed by the constraining layer increases, ultimately causing the actuator to lose its effective winding and grasping capability.

Changes in pleat spacing (g) or pleat width (b) have effects opposite to those associated with increasing pleat height. Specifically, increasing either pleat spacing or pleat width produces a deformation trend similar to that caused by decreasing the pleat height (h). This is because, when all other parameters—including the number of pleats—are held constant, variations in pleat spacing, pleat width, or pleat height primarily alter the unfolded length of the pleated bladder perpendicular to the pleats. If only the pleat spacing or pleat width is changed while the number of pleats remains constant, the length of the pleated region perpendicular to the pleats also increases. However, the difference between this length and the unfolded length of the pleated bladder remains unchanged, and therefore the central angle of the deformed actuator remains approximately constant. Nevertheless, because the length of the pleated region increases, the radius of the circle enclosed by the constraining-layer bladder also becomes larger. This configuration may therefore be more suitable for winding and grasping objects with larger diameters.

To further clarify how structural parameters influence winding and attachment deformation, the feasible ranges and interrelationships of the key geometric parameters in a simplified actuator model were analyzed. A finite element model of the actuator (Supplementary Figure 1C) was then established in ABAQUS 6.14. Contact interactions were defined among the actuator components. The elastic modulus was obtained by averaging the warp and weft values measured in the fabric mechanical tests. The material density was calculated from the areal density and thickness of the fabric, and the Poisson's ratio was set to 0.3 according to the literature. The model employed shell elements with a predominantly quadrilateral mesh and a mesh size of 0.8 mm. The element type was a four-node curved thin shell with reduced integration, hourglass control, and finite membrane strain capability. Overall, the mesh exhibited uniform distribution, regular element shape, orderly arrangement, and satisfactory quality.

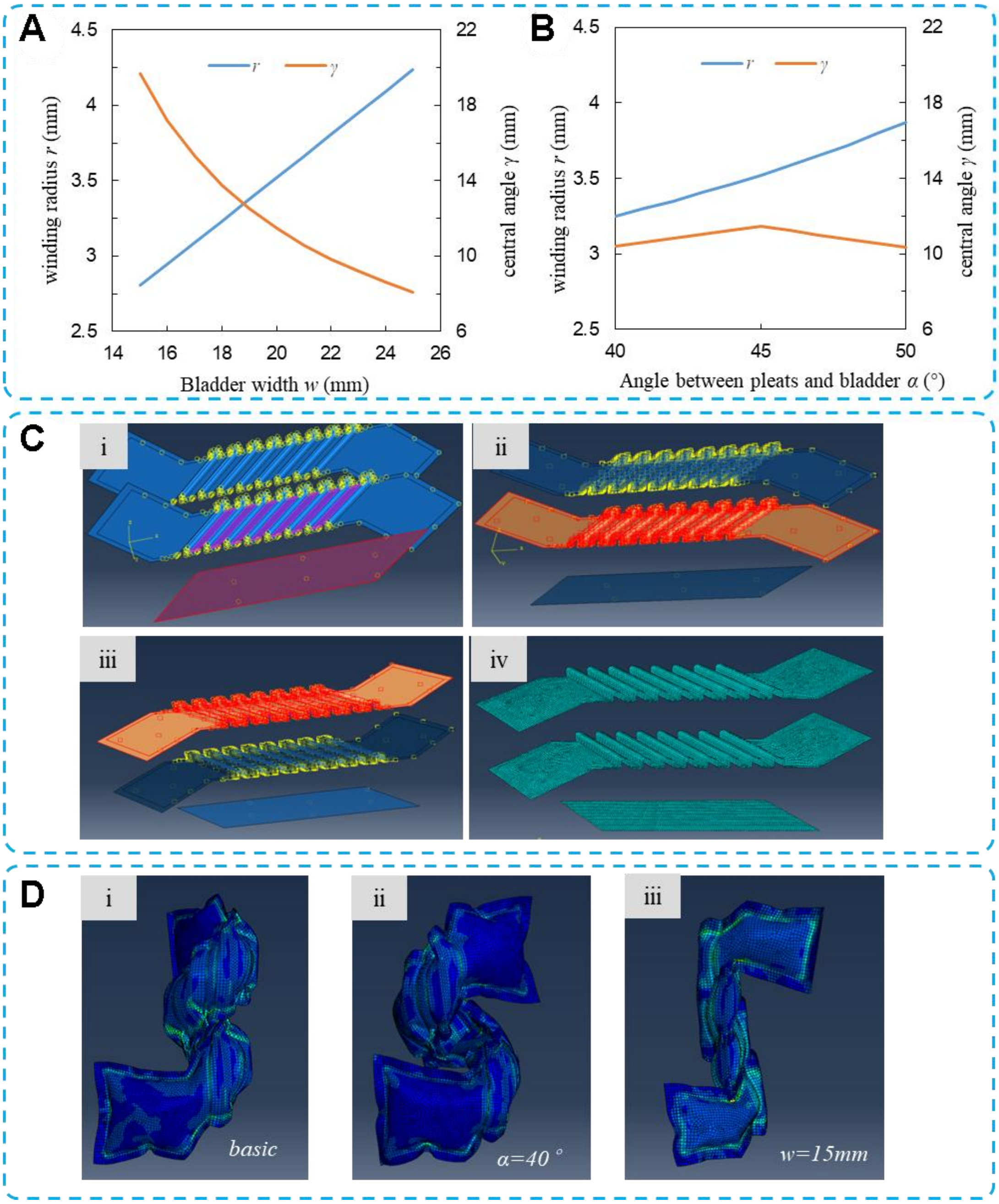

Supplementary Figure 1. Influence of actuator structural parameter variations on deformation and simulation modeling analysis. (A) Effect of bladder width variation on actuator deformation; (B) Effect of pleat inclination angle variation on actuator deformation; (C) Finite element model assembly and contact settings (i: contact setting between bladder and restraining layer; ii: contact setting for bottom layer fabric of bladder; iii: contact setting for top layer fabric of bladder; iv: finite element model mesh); (D) Finite element simulation of winding deformation for actuators with different structural parameters.

Deformation results from models with different parameters were analyzed and compared (Supplementary Figure 1D): Model 1 employed the baseline parameters that satisfy the optimal performance design requirements: pleat-bladder angle α =45°, bladder width w=20mm, pleat spacing g=5mm, pleat height h=3.9mm, pleat width b=2.5mm, and number of pleats n=8. Based on this ideal parameter set, specific parameters were modified in other models: In Model 2, the pleat-bladder angle was reduced to α =40°, relative to Model 1. In Model 3, the bladder width was reduced to w=15mm relative to Model 1. The simulation and physical prototype deformation results indicated: 1) The baseline parameter actuator (Model 1) deformed well, exhibiting desirable deformation characteristics. The lead of its cylindrical helix equaled the length of the inflated bladder along the pleat direction. Adjacent coils made contact precisely at the heat-sealed regions without interference. This indicates that the actuator's deformation simultaneously reached both limits – the minimum radius of the restraining layer circle (due to full pleat expansion) and the minimum lead – satisfying the ideal deformation design criterion. 2) For Model 2 (α =40°), the finite element simulation showed that the actuator deformation did not reach the minimum lead, and the enveloping central angle after deformation was smaller co MPared to Model 1. This aligns with the previously discussed effect of reducing the pleat-bladder angle. 3) For Model 3 (w=15mm), the simulation results demonstrated a significant decrease in the radius of the restraining layer's cylindrical helix and a substantial increase in the enveloping central angle, corresponding to a greater number of winding turns. These findings are consistent with the theoretical discussion on the effect of reducing bladder width, thereby validating the correctness of the theoretical model regarding the influence of parameter changes on actuator deformation.

Supplementary Section 2. Mechanical property test of nylon fabric

In this study, double-sided TPU-coated nylon woven fabric was selected for fabrication of the FAWA. This material has a three-layer structure consisting of a woven textile core that provides mechanical strength and TPU coatings on both sides that ensure airtightness. Upon heating, the TPU softens and melts, thereby enabling heat-sealing during fabrication. To quantitatively compare the mechanical properties of candidate fabrics, tensile and bending-stiffness tests were conducted on 20D woven fabric (TPU coating 0.03 mm, total thickness 0.1 mm, areal density 118 g/m², Jiaxing Inch Eco-Materials) and 40D woven fabric (TPU coating 0.06mm, total thickness 0.19mm, areal density 222 g/m², Jiaxing Inch Eco-Materials). Bending stiffness is widely used as an indicator of fabric flexibility. Fabrics outside this denier range were not examined because preliminary experiments showed that fabrics below 20D, although advantageous for lightweight construction, had insufficient tear resistance and made the resulting FAWAs susceptible to damage. By contrast, fabrics above 40D were excessively stiff; although they might offer higher load-bearing capacity, they required unacceptably high driving pressures and were therefore inconsistent with the present design objectives.

a) Tensile Test [1]: Fabric samples were cut into standard specimens of 260 mm × 50 mm. Tensile tests (Supplementary Figure 2A) were conducted using a tensile testing machine (Yangzhou JING ZHUO Test Machinery Factory) with a gauge length of 200 mm and a testing speed of 100 mm/min. The elastic modulus was calculated as $E=\frac{\sigma}{\varepsilon}$ (where E is the elastic modulus, σ is stress, and ε is strain). As shown in Supplementary Figure 2B, the 40D nylon woven fabric exhibited an elongation of 23.1% at a force of 323.4 N (E=147 MPa) in the weft direction, and an elongation of 21.7% at 568.8 N (E=276 MPa) in the warp direction. The 20D nylon woven fabric showed an elongation of 32.7% at 231.3 N (E=141 MPa) in the weft direction, and an elongation of 22.1% at 264.6 N (E=239 MPa) in the warp direction. The results indicate that the elastic moduli of the two fabrics are relatively similar. However, the higher denier fabric is thicker, consequently stiffer, and capable of withstanding higher loads. Furthermore, both fabrics were stiffer in the warp direction.

b) Bending Stiffness Test (Inclined Plane Method) [2]: Standard fabric specimens measuring 25 mm × 250 mm were placed on a horizontal platform connected to an inclined plane. The short edge of the fabric strip was aligned with the edge of the horizontal platform. The angle between the inclined plane and the horizontal platform, denoted as θ, is adjustable. A steel ruler was placed on top of the specimen, aligned with its short edge. The ruler was gently pushed, sliding the fabric strip towards the inclined plane until the overhanging end of the strip touched the inclined plane (Supplementary Figure2C). The sliding distance (l) of the fabric strip was recorded. The fabric bending rigidity was calculated using the following formulas [2]:

$$C=l\left(\frac{\cos\frac{1}{2}\theta}{8\tan\theta}\right)^{\frac{1}{3}} \quad \text{(S2)}$$

$$B=\rho*\ C^{3}*\ 10^{-3} \quad \text{(S3)}$$

where C is the average bending length of the fabric (cm), B is the bending rigidity (mN·cm), and ρ is the fabric areal density (g/m²). In this test, θ was set to 41.5°. At this specific angle, the bending length C equals half the sliding distance l, simplifying subsequent calculations. As shown in the fabric bending property test results (Supplementary Figure 2D), the 20D fabric exhibited a weft bending rigidity of 0.580 mN·cm and a warp bending rigidity of 0.688 mN·cm. The 40D fabric showed a weft bending rigidity of 4.370 mN·cm and a warp bending rigidity of 4.616 mN·cm. These results indicate negligible difference between warp and weft bending rigidity, suggesting the fabric can be considered isotropic with respect to this property.

Moreover, the bending rigidity of the 20D nylon woven fabric was substantially lower than that of the 40D fabric, indicating that the 20D material is softer and more flexible. Bladders fabricated from the 20D fabric can therefore inflate and deform more readily under lower pressure and exhibit greater compliance during contact with target objects. For adhesive applications, substrate stiffness has an important influence on interfacial performance; in general, a softer substrate with lower stiffness tends to provide stronger adhesion. For this reason, all FAWA samples investigated in this study were fabricated from 20D nylon woven fabric.

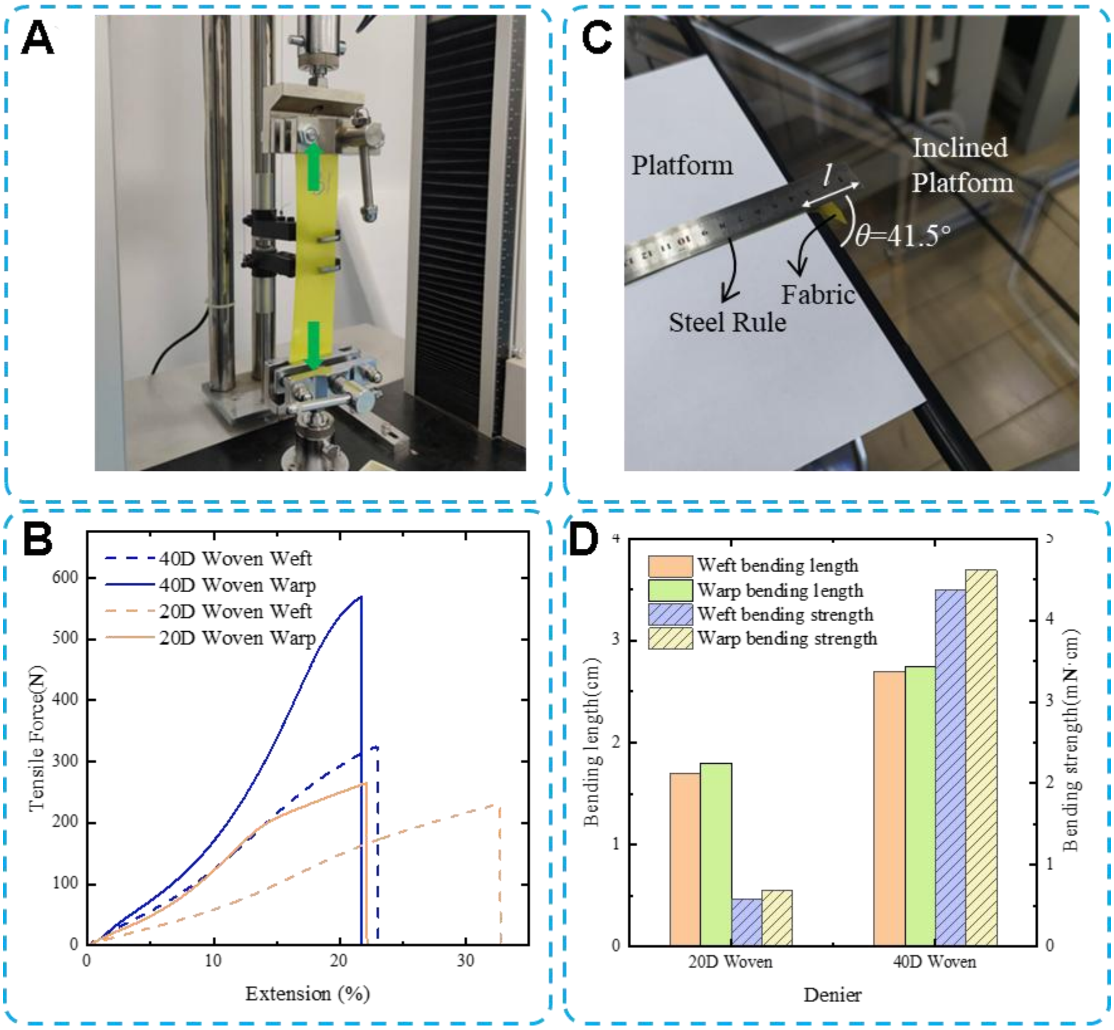

Supplementary Figure 2. Fabric performance testing. (A) Fabric tensile property test setup. (B) Fabric tensile property results. (C) Fabric bending stiffness test setup. (D) Fabric bending property results.

Supplementary Section 3. Effect of Fabric Properties on the Adhesive Winding Performance of the Actuator

Based on the preceding investigation of the mechanical properties of the fabrics, this section further analyzes their influence on the adhesive winding performance of the actuator. Bio-inspired adhesive winding actuators with the baseline structural parameters were first fabricated using 20D and 40D nylon woven fabrics, respectively. The axial adhesive winding performance of the actuators was then evaluated using the bio-inspired adhesive winding actuator performance test platform. After inflation, the actuator wound around an acrylic tube with a diameter of 11 mm. The actuator pressure was set within the range of 30-80 kPa, starting from 30 kPa and increasing in increments of 10 kPa. Driven by the two-dimensional translation platform, the acrylic tube moved upward at a feed speed V_f of 50 mm/min. During this process, the force sensor data were recorded, and the peak force was taken as the maximum axial adhesive winding force. To reduce experimental error, each experiment was repeated three to five times; the same procedure was adopted for the experiments described below. The experimental results are shown in Supplementary Figure 3.

The actuator fabricated from 20D nylon woven fabric exhibited excellent axial adhesive winding performance. At an air pressure of 30 kPa, it could withstand a maximum load of approximately 14 N. As the pressure increased, its maximum load capacity rose steadily. At 50 kPa, the maximum load was approximately 22 N, and at 80 kPa it reached approximately 30 N. Moreover, the axial adhesive winding capacity showed a good linear relationship with pressure, indicating that the actuator had stable adhesive winding capability.

By contrast, the actuator fabricated from 40D nylon woven fabric could withstand only approximately 5 N at 30 kPa and only approximately 10 N even at 80 kPa. In addition, the axial adhesive winding force did not show a clear linear relationship with pressure, indicating unstable axial adhesive winding performance. In summary, the actuator fabricated from 20D woven fabric exhibited significantly stronger and more stable adhesive winding performance than the actuator fabricated from 40D woven fabric.

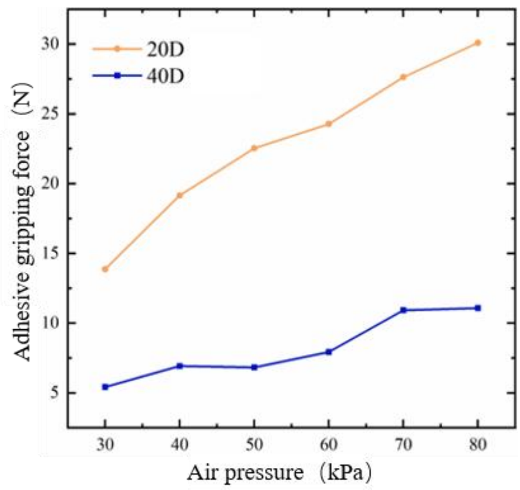

Supplementary Figure 3. Axial adhesive winding performance test results for actuators fabricated from different fabrics.

From the perspective of material mechanical properties, two factors affect the adhesive winding performance of the actuator: the substrate stiffness of the actuator and the adhesive preload generated by the actuator. As tested in the previous section, the 20D woven fabric is softer and has a significantly lower stiffness than the 40D woven fabric. Because of the special deformation state of the bio-inspired adhesive winding actuator, accurate measurement of the adhesive preload is relatively complex and difficult. Therefore, in this section, the tip blocking force of the actuator was used to characterize the adhesive preload.

Although the tip blocking force cannot be directly equated with the adhesive preload, both quantities essentially represent forces generated when actuator deformation is constrained. Under identical structural parameters, deformation behavior, and driving pressure, a proportional relationship can be expected between them. Tip blocking force has been commonly employed as a measure of performance for fabric-based pleated-bladder soft robots [3,4]; accordingly, employing it to characterize the adhesive preload is a valid approach.

As shown in Supplementary Figure 4A, the tip blocking force of actuators fabricated from woven fabrics with different parameters was tested. The proximal end of the actuator was fixed, its back side was supported by a base platform, and a force sensor was placed at the distal end. A gap was left between the force sensor and the base platform, with a width approximately equal to the thickness of the actuator after inflation. The actuator was inflated over a pressure range of 30-80 kPa, starting from

30 kPa and increasing in 10 kPa increments. Under pneumatic actuation, the actuator tended to bend, but the experimental setup constrained its deformation. The force exerted by the actuator on the force sensor under this constrained condition was defined as the tip blocking force, whose direction was perpendicular to the force sensor.

The experimental results are shown in Supplementary Figure 4B. The actuator fabricated from 20D nylon woven fabric produced a slightly larger tip blocking force than that fabricated from 40D nylon woven fabric. It should be noted that the 30 kPa and 40 kPa tip blocking force data for the 40D nylon woven fabric actuator are absent because the 40D fabric was relatively stiff and, under the constraints of the experimental setup, could not undergo winding or curling deformation. At lower pressures, the pleats could not unfold, thereby obstructing airflow.

In summary, the difference in tip blocking force between actuators fabricated from the two woven fabrics was relatively small, whereas the difference in maximum axial adhesive winding performance was substantial. This indicates that substrate stiffness is the main factor affecting the adhesive winding performance of the actuator: the softer the substrate, the stronger the adhesive winding performance. Based on this analysis, 20D nylon woven fabric was selected for fabricating the bio-inspired adhesive winding actuator, and the subsequent analysis is based on this material.

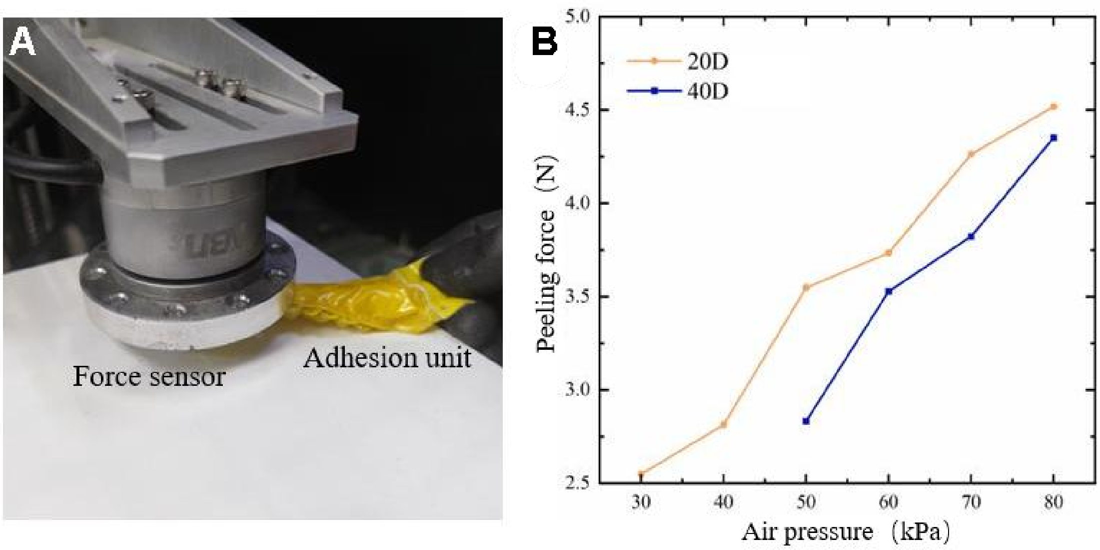

Supplementary Figure 4. Tip blocking force test and results of the actuator. (A) tip blocking force test of the actuator; (B) tip blocking force test results.

Supplementary Section 4. Functional Parameters of the Bio-inspired Adhesive Winding Actuator Performance Test System

To evaluate the axial adhesion and winding performance of the actuator, a dedicated testing platform for the bioinspired adhesive winding actuator was constructed. The platform consisted of a two-dimensional translation mechanism, a small vise, a force sensor, and a miniature portable pneumatic system. More specifically, the FAWA test setup included two orthogonal moving rails along the x- and z-directions, small vise, a force sensor, and the portable pneumatic actuation unit. The force sensor used in the platform was a GJBLS-I single-axis force sensor manufactured by Bengbu Gaojing Sensor Co., Ltd. (specifications are listed in Table S1). Signal acquisition was performed using an NBIT-DUS-2404A 24-bit parallel analog data-acquisition card with a USB 2.0 interface, integrating signal conditioning, acquisition, and transmission functions (parameter settings are summarized in Table S2), manufactured by Nanjing SYNWIT Sensor Technology.

The hardware architecture of the miniature portable pneumatic system is shown in Supplementary Figure 5A. The system mainly consists of an Arduino Uno controller, a DC motor speed-control board, a miniature air pump, relays, solenoid valves, a pressure sensor, and voltage-regulation modules. The Arduino Uno development board is based on the ATmega328P microcontroller and provides convenient hardware interfacing and straightforward software implementation. The DC motor speed-control board receives PWM signals from the Arduino and regulates the voltage supplied to the air pump according to the PWM duty cycle, thereby controlling pump speed and output pressure. Three OST solenoid valves were used: two 3/2-way valves and one 2/2-way valve, with response times below 10 ms and an operating frequency of 30 Hz. The relays receive control signals from the Arduino and switch the solenoid valves on or off, thereby changing the operating state of the pneumatic circuit. The pressure sensor, with a measurement range of -100 to 300 kPa, monitors the circuit pressure and feeds the signal back to the controller. The control board compares the measured pressure with the prescribed setpoint and adjusts the PWM duty cycle using a PID algorithm, thereby enabling closed-loop pressure regulation. By switching the valve states, the pneumatic circuit can realize positive-pressure actuation, negative-pressure actuation, pressure holding, and venting functions (Supplementary Figure 5B). The positive-pressure valve and negative-pressure valve are both 3/2-way solenoid valves, whereas the vent valve is a 2/2-way solenoid valve. In the de-energized state, the valve ports connected to the air pump are open to the atmosphere, while the vent valve remains closed. The valve logic and the corresponding pneumatic functions are summarized in Table S3, where "On" denotes the energized state and "Off" denotes the de-energized state.

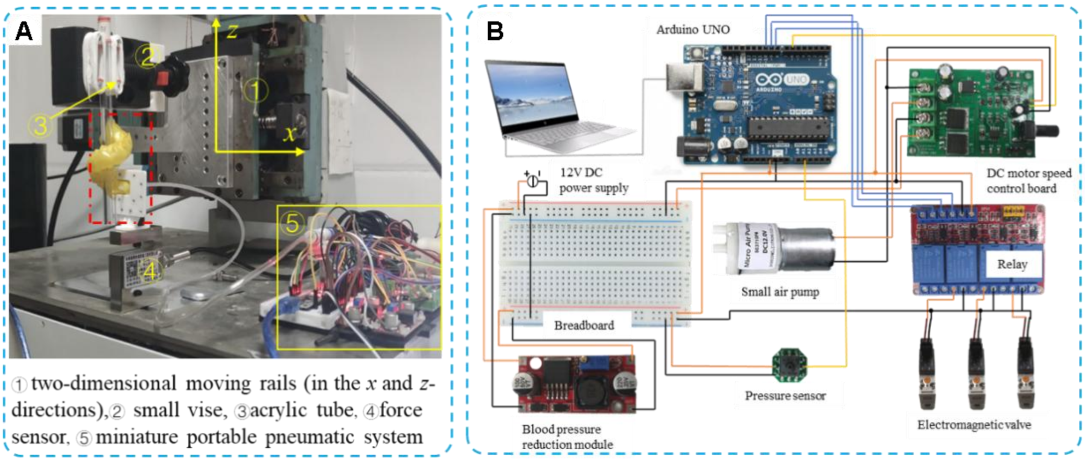

① two-dimensional moving rails (in the x and z-directions), ② small vise, ③ acrylic tube, ④ force sensor, ⑤ miniature portable pneumatic system

Supplementary Figure 5. Schematic diagram of the bio-inspired adhesive winding actuator performance test platform. (A) Adhesion and winding force test platform. (B) Pneumatic system circuit connection diagram.

Supplementary Table 1. Force sensor technical specifications

Parameter	Specification
Range (kg)	±5
Sensitivity (mV/V)	2.0±0.05
Nonlinearity (%F·S)	≤0.03
Repeatability (%F·S)	≤0.03

Supplementary Table 2. Parameter settings for the force acquisition system

Parameter	Specification
Acquisition Resolution	24-bit
Sampling Rate	10KS/s
Amplification Factor	250
Measurement Range	-12.5mV～12.5mV

Supplementary Table 3. Solenoid valve working state design for the pneumatic system

Positive Pressure	Negative Pressure	Vent	Pneumatic Circuit State
On	Off	Off	Positive Pressure
Off	On	Off	Negative Pressure
Off	Off	Off	Pressure Holding
Off	Off	On	Venting

Supplementary Section 5. Battery Capacity and Theoretical Endurance Analysis

At the present stage, the FAWA rod-climbing robot prototype is powered mainly by an external regulated laboratory power supply, and an onboard battery module has not yet been integrated. Therefore, this section provides only a theoretical estimate of the endurance capability under onboard battery operation. According to the prototype configuration and the climbing task requirements, the total power consumption mainly arises from the leg servos, pneumatic system, auxiliary control circuitry, and power-conversion losses. The robot contains 12 leg digital servos, 8 miniature solenoid valves, and 4 miniature air pumps. During climbing, the robot adopts a tripod gait with a complete gait period of 16 s, and the actuator operating pressure is taken as 50 kPa.

Because the air-pump power directly affects the calculated endurance, and because measured current data for the onboard prototype are not yet available, the single-pump power was selected according to the requirements of 50 kPa pneumatic actuation, co MPact installation, and endurance balance. A nominal single-pump power of Pp= 1.5 W was used as the theoretical calculation baseline, corresponding to a miniature air pump operating at approximately 5 V and 0.30 A:

$$Pp=UpIp=5.0\times0.30=1.50W \tag{S4}$$

For the leg servos, the rated voltage and working current of each servo are 5.5 V and 0.18 A, respectively. Thus, the power of a single servo is 0.99 W, and the total rated power of the 12 servos is:

$$Ps=12\times(5.5\times0.18)=11.88W \tag{S5}$$

For the solenoid valves, the rated voltage and working current of each valve are 5.0 V and 0.10 A, respectively. The power of one solenoid valve is therefore 0.50 W, and the peak power of all eight solenoid valves when energized is:

$$Pv,max=8\times(5.0\times0.10)=4.00W \tag{S6}$$

The auxiliary control circuit, including the controller and signal-acquisition components, is calculated at 5.0 V and 0.20 A, giving a constant power of 1.00 W. The four air pumps are calculated using the selected single-pump power of 1.5 W:

$$Pc=5.0\times0.20=1.00W \tag{S7}$$

$$Ppump,max=4Pp=4\times1.50=6.00W \tag{S8}$$

Therefore, under the peak condition in which all servos, solenoid valves, air pumps, and auxiliary circuits operate simultaneously, the total peak power is:

$$P_{max}=P_s+P_{v,max}+P_{pump,max}+P_c=22.88W \tag{S9}$$

The average operating power was calculated according to the duty cycle of each component within one complete tripod-gait period. The complete gait period is $T = 16\ s$. The four legs enter the swing phase successively, with a single-leg swing phase of $t_s = 3\ s$. After each swing phase, the robot enters a four-leg support phase of $t_4 = 1\ s$. Therefore, the complete gait period can be expressed as:

$$T=4t_s+4t_4=4\times3+4\times1=16s \tag{S10}$$

For the servos, during each single-leg swing phase, the swing leg moves forward while the other three support legs move backward to drive the body. During the four-leg support phase, all four legs move backward. Therefore, the 12 leg servos participate in posture adjustment or propulsion throughout the complete 16 s cycle, and the duty cycle of the servo system is taken as $D_s = 1$:

$$P_{s,avg}=P_sD_s=11.88\times1=11.88W \tag{S11}$$

For the pneumatic system, each leg contains one air pump and two solenoid valves, which control the pleated bladder and the constraining-layer bladder, respectively. The support phase requires the pleated bladder to maintain positive pressure for adhesive winding; therefore, the main pressurization time of the pleated bladder for a single leg is the non-swing period, namely 16 - 3 = 13 s. The constraining-layer bladder mainly inflates during the latter part of the swing phase to release and extend the actuator, and this duration is approximated as 1.5 s. Accordingly, the effective pneumatic duty cycle of a single leg is:

$$D_{air}=(13+1.50)/16=0.906 \tag{S12}$$

Since the robot has four independent pneumatic circuits, the average solenoid-valve power is calculated by weighting the working durations of the four pleated-bladder valves and four constraining-layer-bladder valves:

$$P_{v,avg}=4P_{v1}\times13/16+4P_{v1}\times1.50/16 \tag{S13}$$

$$P_{v,avg}=4\times0.50\times(13+1.50)/16=1.81W \tag{S14}$$

The air pumps work when the corresponding pneumatic circuits need to establish or maintain positive pressure. Therefore, the average power of the four air pumps is:

$$P_{pump,avg}=4P_pD_{air}=4\times1.50\times0.906=5.44W \tag{S15}$$

The auxiliary control circuit operates continuously throughout the entire cycle, and its average power is 1.00 W. Therefore, the average operating power of the robot based on tripod-gait duty-cycle calculation is:

$$Pavg=Ps,avg+Pv,avg+Ppump,avg+Pc \tag{S16}$$

$$Pavg=11.88+1.81+5.44+1.00=20.13W \tag{S17}$$

To address the reviewer's concern regarding the continuous current, power, and long-term heating of the onboard pneumatic system, the following calculation is performed within the pneumatic-system power budget rather than treating motor heating as an additional power term. The portion of the pump input power that is not converted into useful pneumatic output is ultimately dissipated as heat. Therefore, the heat generation belongs to the internal energy distribution of *Ppump*,*avg*, while the endurance calculation still uses *Pavg*, which already includes the air-pump input power.

According to the above duty-cycle calculation, the four air pumps have an average input power of 5.44 W, and the solenoid valves have an average power of 1.81 W. Thus, the equivalent average current and average power on the 5 V pneumatic-system bus are:

$$Pair,avg=Ppump,avg+Pv,avg=5.44+1.81=7.25W \tag{S18}$$

$$Iair,avg=Pair,avg/5.0=7.25/5.0=1.45A \tag{S19}$$

It should be emphasized that 1.45 A is the equivalent average current of the entire 5 V pneumatic system, not the continuous current of a single air pump. Of this value, the four pumps account for approximately 1.09 A in total, whereas the solenoid valves account for approximately 0.36 A in total. When this pneumatic-system demand is converted to the 11.1 V battery side with a voltage-regulator efficiency of ηd = 0.85, the corresponding average battery-side current is approximately:

$$Ibat,air=Pair,avg/(11.1\eta d)=7.25/(11.1\times0.85)=0.77A \tag{S20}$$

For the motor-heating issue, let ηm denote the overall energy-conversion efficiency of the air-pump motor and pump body. The equivalent heat load of a single air pump can be expressed as:

$$Pheat,1=(1-\eta m)PpDair \tag{S21}$$

In the absence of measured efficiency data, ηm = 0.25 was adopted as a conservative estimate. The equivalent heat load of a single air pump is then:

$$Pheat,1=(1-0.25)\times1.50\times0.906=1.02W \tag{S22}$$

This heat load is not an additional power term for the endurance calculation; instead, it is the heat-dissipation portion of the average air-pump input power. Using the thermal-resistance model $\Delta T = R\theta Pheat,1$, and taking an ambient temperature of 25 °C and an allowable pump-shell temperature of 80 °C as preliminary boundaries, the maximum allowable equivalent thermal resistance of a single air pump is:

$$R\theta,max=(80-25)/1.02=53.9°C/W \tag{S23}$$

Therefore, if the selected miniature air pump can operate continuously near 5 V and 0.30 A, and if the mounting structure provides an equivalent thermal resistance lower than approximately 54 °C/W, excessive overheating can theoretically be avoided. If the pump is fully enclosed in a narrow space, a temperature-rise experiment is still required for final verification.

In the endurance calculation, the number of operating cycles under ideal conditions is not reported separately. Instead, voltage-regulator efficiency, battery cut-off voltage, wiring loss, and usable-capacity degradation are incorporated together. For a 3S lithium battery with a nominal voltage of 11.1 V and a capacity of 1000 mAh, the nominal battery energy is:

$$Eb=UbCb=11.1\times1.00=11.1Wh \tag{S24}$$

A combined usable factor of 0.85 × 0.85 was adopted to account for power-conversion efficiency and usable-capacity reduction. The effective battery energy is:

$$Euse=Eb\times0.85\times0.85=11.1\times0.85\times0.85=8.02Wh \tag{S25}$$

Equivalently, this loss can also be represented as a total equivalent power demand on the battery side:

$$Pall=Pavg/(0.85\times0.85)=20.13/0.7225=27.86W \tag{S26}$$

Therefore, after accounting for all power-conversion losses and usable-capacity degradation, the continuous operating time of the robot and the corresponding number of complete tripod-gait cycles are:

$$teng=Euse/Pavg=8.02/20.13=0.398h\approx23.9min \tag{S27}$$

$$Neng=teng\times3600/16\approx90 \tag{S28}$$

In summary, when the onboard battery capacity is 11.1 V/1000 mAh and the single-pump power is taken as 1.5 W, the peak power of the robot is approximately 22.88 W, and the average operating power calculated from the tripod-gait duty cycle is approximately 20.13 W. The onboard pneumatic system requires an equivalent average current of approximately 1.45 A and an average power of approximately 7.25 W on the 5 V bus to maintain 50 kPa operation. Here, 1.45 A refers to the average current of the entire pneumatic system rather than a single air pump. Air-pump heating is already included in the air-pump input power and is not added again as an extra power term in the endurance calculation. Under the conservative efficiency estimate, the equivalent heat load of a single air pump is approximately 1.02 W. If basic thermal paths are reserved in the mounting structure, uncontrollable overheating is not expected theoretically, although final validation still requires temperature-rise testing. After accounting for power-conversion efficiency and usable-capacity degradation, the engineering endurance of the robot is approximately 23.9 min, corresponding to about 90 complete tripod-gait cycles. This result can be used as a preliminary reference for onboard battery and pneumatic-system selection, while the final endurance and pump temperature rise should be calibrated experimentally by measuring the battery-terminal voltage/current and the motor-shell temperature during actual climbing operation.

Supplementary Section 6. Representative Cyclic Reusability Test of FAWA

To provide a preliminary evaluation of cyclic reuse, a representative repeated adhesive-winding test was conducted using the baseline FAWA on a 10 mm diameter acrylic rod at 50 kPa. The peak adhesive-winding force was recorded over 100 consecutive cycles. As shown in Supplementary Figure 6, the peak force was initially maintained at approximately 20–22 N. After repeated cycling, the force decreased moderately and then gradually stabilized at approximately 17–18 N. These results indicate that, under this representative operating condition, FAWA can maintain substantial adhesive-winding capacity after repeated attachment–detachment cycles. This test provides preliminary support for cyclic reuse, although more extensive durability evaluation under different pressures, rod diameters, and surface conditions will be required in future work.

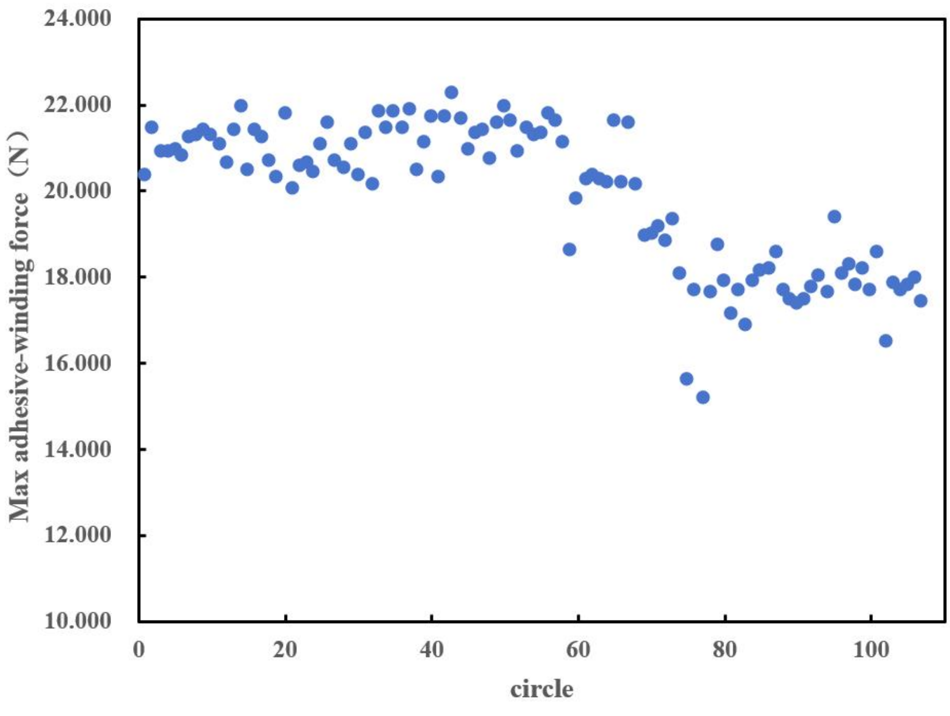

Supplementary Figure 6. Peak adhesive-winding force of FAWA over 100 repeated adhesive-winding cycles on a 10 mm diameter acrylic rod at 50 kPa.

REFERENCES

1. State Administration for Market Regulation, Standardization Administration of China. GB/T 3923.1-2013 Textiles—Tensile properties of fabrics—Part 1: Determination of maximum force and elongation at maximum force using the strip method[S]. Beijing: China Standards Press, 2013. (in Chinese)
2. State Administration for Market Regulation, Standardization Administration of China. GB/T 18318.1-2009 Textiles—Test method for bending property—Part 1: Cantilever method[S]. Beijing: China Standards Press, 2009. (in Chinese)
3. Ge L, Chen F, Wang D, et al. Design, modeling, and evaluation of fabric-based pneumatic actuators for soft wearable assistive gloves. Soft Robot 2020;7(5):583–596; doi: 10.1089/soro.2019.0105.
4. Feng M, Yang D, Gu G. High-force fabric-based pneumatic actuators with asymmetric chambers and interference-reinforced structure for soft wearable assistive gloves. IEEE Robotics and Automation Letters, 2021, 6(2): 3105-11; doi: 10.1109/LRA.2021.3062588